

Mechanism to transfer linear momentum from a Surface Acoustic Wave to a Magnetic Domain Wall

Alejandro Rivelles¹, Rocío Yanes³, Luis Torres³, Rodrigo Guedas^{1,2}, Raúl Izquierdo-López^{1,4}, Marco Maicas¹, Maria del Mar Sanz¹, Jorge Pedrós^{1,4}, Fernando Calle^{1,4}, Luis López-Díaz³, Jose Luis Prieto¹

1 Instituto de Sistemas Optoelectrónicos y Microtecnología (ISOM), Universidad Politécnica de Madrid, Madrid, Spain.

2 SPINTEC, University of Grenoble Alpes, CNRS, CEA, Grenoble, France.

3 Applied Physics Department, Universidad de Salamanca, Salamanca, Castilla y León, Spain.

4 Department of Electric Engineering, ETSI Telecomunicación, Universidad Politécnica de Madrid, Madrid, Spain.

Abstract

Surface Acoustic Waves (SAW) have been used frequently in spintronic applications, mostly to decrease the magnetic field or the electric current required to move magnetic domain walls (DW). Because the SAW cannot achieve magnetic switching without the assistance of a magnetic field or a current, for a marginal improvement in the energy required for the magnetic switching, the device gains in complexity, making it impractical. In this work, we report a mechanism that allows a transfer of linear momentum from the acoustic wave to the magnetic domain wall. Experimentally we show that, using the appropriate dimensions of the magnetic strip, the SAW can move the DW in the same direction as the traveling SAW. With the help of micromagnetic simulations, we reveal a complex yet direct mechanism that allows the SAW to push the DW in the same direction of its travel, even without any external field or currents. The DW can reach velocities in the range of 100 m/s and at a very small energetic cost, equivalent to using a current density of $\sim 5 \cdot 10^4$ A/cm² if the movement was triggered by spin transfer. This new mechanism opens the door to designing innovative spintronic devices where the magnetization can be controlled exclusively by an acoustic wave.

Introduction

Magnetostriction is a property of magnetic materials through which its magnetic properties can be altered using mechanical stress. This property is at the core of several widespread applications such as underwater sonar¹, security labels,² and magnetic sensors³. The field of spintronics has also explored the possibilities of magnetoelastic interactions through numerous experiments, often using a Surface Acoustic Wave (SAW)⁴. Weiler *et al.*⁵ showed that an elastic wave could lead to an acoustic-driven ferromagnetic resonance (FMR) in a Nickel film. The same authors also produced a pure spin current and measured magnetoelastic spin pumping⁶. The SAW can assist the magnetic switching of a ferromagnetic film⁷ or of a nano-element^{8,9}, it can reduce the energy required for magnetic recording¹⁰ or even decrease the energy dissipation in spin-transfer-torque random access memories¹¹. More recently, a SAW was used to achieve an ordered generation of magnetic skyrmions¹². In spintronic devices that rely on the control of the magnetic domain wall (DW) motion, the interaction with a SAW can facilitate the movement of the DW and decrease the electric current^{13,14,15,16} required for operation, which often leads to detrimental thermal effects^{17,18}. There is also a theoretical work proposing the use of an acoustic standing wave to control the movement and position of a DW¹⁹.

Despite the amount of research devoted to the interaction of a SAW with a magnetic device, the goal of moving a DW in the direction of the traveling SAW, reliably and without any external magnetic field or electric current, has not been achieved so far. As the SAW is a harmonic symmetric oscillation, one should not expect a net unidirectional DW movement: the DW would move forward half of the SAW cycle and, the same distance backward, the other half. Very recently Yang *et al.*²⁰ reported that, in the presence of an out-of-plane magnetic field, a skyrmion could be occasionally moved under the action of a shear horizontal acoustic wave. At best, the skyrmion would move 37% of the attempts in small steps equivalent to speeds in the range of $\mu\text{m/s}$. Therefore, this result does not hide a fundamental mechanism that can move a DW reliably and at sizable speeds in the direction of the SAW, without a magnetic field or current.

In this work, despite the expectations, we show that a SAW can indeed move a DW in only one direction, that of the traveling SAW. In DWs sufficiently wide (in the range of a quarter of the wavelength of the SAW), we found experimental evidence of directional assistance of the SAW to the movement of the DW. Through the micromagnetic simulations performed to fit the experimental results, we unlock an innovative mechanism through which the SAW (an acoustic wave) transfers linear momentum to the DW (a magnetic element). During the half cycle of the acoustic wave, the DW reduces its width, accumulating energy. When this energy becomes sufficiently large, the DW jumps forward to release some of the magnetoelastic stress through an internal wave. This makes the two cycles of the SAW different from the perspective of the DW and the result is a net movement in the direction of the SAW. Within the weak pinning regime, the SAW can displace the DW without a magnetic field or an electric current, achieving velocities larger than 100 m/s. The power required for this movement is very small, ~ 0.2 nW, equivalent to using $\sim 10^4$ A/cm² if the DW was moved by spin transfer. This novel mechanism could be the base of future optimized spintronic devices, as it will not require fields or electric currents to control the DW's movement, allowing easy device integration and avoiding any thermal issues associated with the electric current.

Experimental Results

The device configuration used for the main experiment is sketched in Fig. 1a. Two sets of Interdigital Transducers (IDT) are deposited over a 128° Y-cut LiNbO₃ substrate, both designed to resonate at 1.3 GHz for the Rayleigh mode. A magnetic strip sits in the middle of the two IDTs, as shown in the inset to Fig. 1a. The structure of the magnetic strip is

Ta(1nm)/Fe₆₅Co₃₅(3nm)/Ni₈₀Fe₂₀(5nm)/Pt(2nm), and it is 1 μm wide and 20 μm long. Notice that the NiFe layer is not magnetostrictive but increases the AMR signal from the DW, facilitating its detection. The magnetic strip is contacted by a central line and two lateral contacts with the structure Cr(10nm)/Au(70nm). The nucleation of a pair of magnetic domain walls is achieved by delivering a pulse of current through the central current line^{21,22,23}. The presence of the DW can be measured in the lateral contact by the drop in the anisotropic magnetoresistance (AMR) associated with the DW^{24,25}.

The experiment described in this section is based on monitoring the probability of detecting the presence of a DW in the strip, for different external magnetic fields and in the presence of the SAW. To nucleate a DW, the external magnetic field is ramped to a large negative saturating value and then set to a smaller value called the ‘injection field’, H_{inj} . Once H_{inj} is stabilized at a given value, a short current pulse is delivered through the central line as shown in the inset to Fig. 1a. If this current pulse has enough amplitude²⁶ it nucleates an inverted domain under the central conductive line with a DW on each side. This is a very standard DW nucleation procedure often used in spintronic experiments^{22,24}. When the DW is nucleated, the resistance of the strip decreases slightly due to AMR associated with the DW²⁵. By repeating this nucleation procedure many times for $H_{inj}=0$, we can build a histogram with the typical resistance values associated with the DW, as shown in Fig. 1b. The typical resistances for $H_{inj}=0$ are found around 0.25 Ω and 0.32 Ω. To image the structure of the nucleated DW, the sample was taken to the MFM after the DW was nucleated and its resistance recorded. Figs. 1c and 1d, show that the structure of the DW is always transversal, with a slightly larger width in the DW associated with a larger AMR value. All the DWs observed in this work have always been transversal, such as the ones shown in Figs. 1c and 1d. It is worth noticing that the MFM image also reveals some magnetic microstructure in the rest of the strip (see also Fig. S1 in Supplementary Information), due to the polycrystalline nature of the FeCo layer.

The nucleation procedure is repeated 100 times for each value of H_{inj} . If all the events lead to the resistance change associated with a DW, we would consider that, for that value of H_{inj} , the probability of injecting a DW is one. Repeating the 100 measurements for each H_{inj} , we build a probability plot like the one shown in Fig. 1e. For positive values of H_{inj} , the DW is always detected until a value of 15 Oe is reached and then, the probability of detecting the DW drops to zero. For $H_{inj}>15$ Oe, the external field is larger than the DW propagation field and the DW, once nucleated, travels toward the ends of the strip to complete the magnetic reversal (see also the section on micromagnetic simulations). The DW can still be nucleated for a small negative H_{inj} although, for $H_{inj}<-7$ Oe, the probability drops again to zero. For H_{inj} more negative than -7 Oe, the DWs, if nucleated, would travel towards each other until the reversed domain disappears (see also the section on micromagnetic simulations).

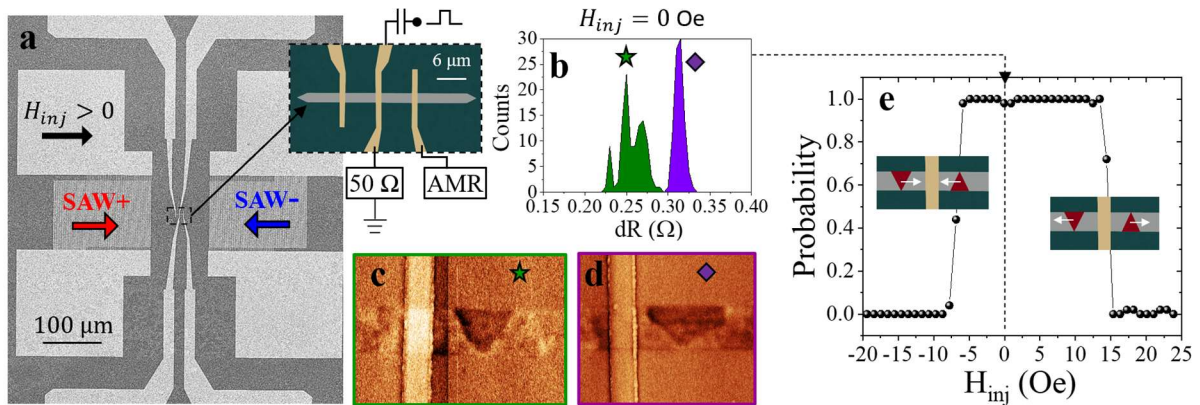


Fig.1. (a) SEM photograph of the device with the two IDTs that can deliver a SAW from left to right (SAW+) and from right to left (SAW-). In the inset, there is a colour-enhanced picture of the strip with the three contacts, where the middle one is used to nucleate the DWs and the lateral ones are used to measure the AMR of the DW. (b) Histogram of the

resistance values of 100 nucleation events at $H_{inj}=0$ Oe. The corresponding DW for each resistive peak was imaged by MFM as shown in (c) and (d). (e) Probability plot representing the probability of detecting a DW in the right branch of the strip for different external fields H_{inj} .

The probability plot displayed in Fig. 1e reflects the presence of a DW in the strip (on the right side of the central line) for different external magnetic fields. In Figure 2, we explore the effect that the SAW and its direction of travel have on the probability of detecting a DW in the strip. For $H_{inj}>0$ Oe, Fig. 2a shows that the propagation field (the field at which the probability of detecting a DW goes to zero), decreases in the presence of the SAW. This is to be expected as the vibration of the SAW, enhances the mobility of the DW and its ability to overcome pinning defects¹⁵. Noticeably though, when the SAW travels from left to right (SAW+, red curve in Fig. 2a), the decrease of the propagation field is larger than when the SAW travels from right to left (SAW-, blue curve in Fig. 2a). Note that the measurement is done at the same effective power for the SAW in both directions, so the influence of the central metallic contact on the ferromagnetic strip is taken into account (see Supplementary Information S2). For negative H_{inj} , the effect of the direction of the SAW is opposite to the one described for positive H_{inj} . In this case ($H_{inj}<0$), it is the SAW- the one producing a larger decrease in the probability of detecting the DW (see also some examples of measurements in other devices in Supplementary Information S3).

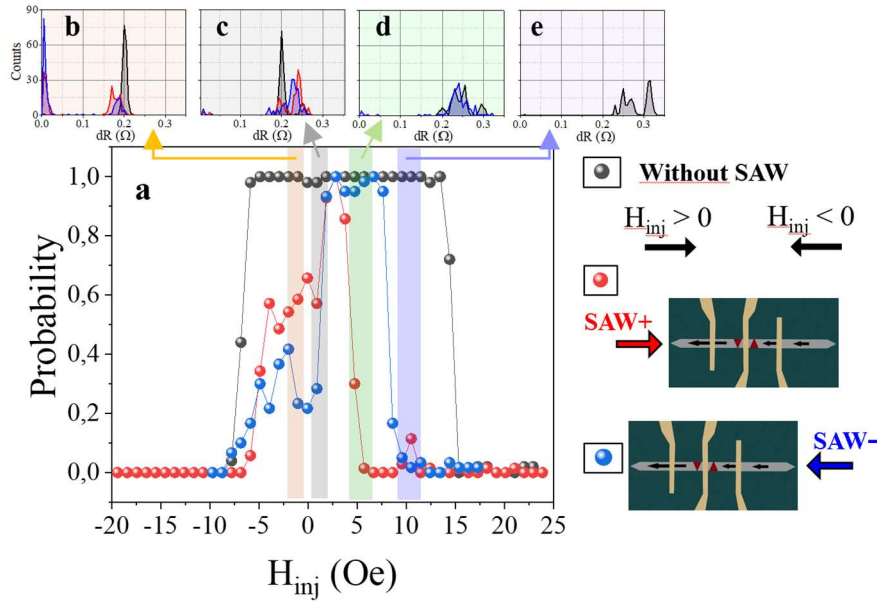


Fig.2. (a) Probability plots of the detection of a DW between the two right contacts of the strip, without SAW (black dots), with a SAW traveling from left to right (red dots), SAW+, as shown in the right-hand side of the figure, and with a SAW traveling from right to left (blue dots), SAW-, as shown in the right-hand side of the figure. In figures b-f, we show histograms of the resistance values recorded for the DWs in the different regions of the field. The color in each histogram corresponds to the direction of the SAW (red corresponds to SAW+ and blue to SAW-). The DW resistance values remain around similar values for the different fields and for the two directions of travel of the SAW.

One possible explanation for the results shown in Fig. 2 is that the SAW affects the structure of the DW, which in turn, changes the propagation field. Experimentally, we have not found any evidence that could justify a change of structure of the nucleated DW when the SAW travels in different directions. The histogram of DW resistance, such as the ones shown in Figs. 2b-2f, shows resistance values very similar to the ones of DWs nucleated without SAW (Fig. 2f), and the structure measured by MFM is always the one of a transversal wall. If we average the histograms taken for all H_{inj} , the average resistance associated with the DW falls within very similar values (see Suppl. Info. S3). Therefore, nucleating the DW in the presence of the SAW does not change the structure of the DW. This fact is also confirmed in the micromagnetic simulations.

The second possibility to explain the results of Fig. 2 is that, through a yet unknown mechanism, the SAW is pushing the DW in the same direction that the SAW is traveling. For instance, SAW+ would push the DWs toward the right, and, in the presence of $H_{inj} > 0$, it would favor the reversal of the strip. Similarly, SAW- would push the DWs towards the left hampering the reversal process, despite the positive H_{inj} . The situation would be the opposite for $H_{inj} < 0$ and the collapse of the reversed domain would be more effective in the presence of SAW- than in the presence of SAW+. In the next section, with the help of detailed micromagnetic simulations, we show that a novel mechanism allows the SAW to push the DW in the direction of the traveling SAW.

Micromagnetic Simulations

All micromagnetic simulations in this work were performed with Mumax 3 software²⁷, where the action of the SAW was included via the magnetoelastic field as explained in Methods. We begin by simulating the experimental system, consisting of a FeCo (3 nm)/Py (5 nm) nanostrip, with dimensions $10 \mu\text{m} \times 1 \mu\text{m}$, positioned on top of a piezoelectric substrate as shown in Fig. 3a. The strip is located between two IDTs where a propagating SAW can be delivered in either direction with a specific frequency and wavelength. See also Methods for further details on the magnetic parameters used in the simulations.

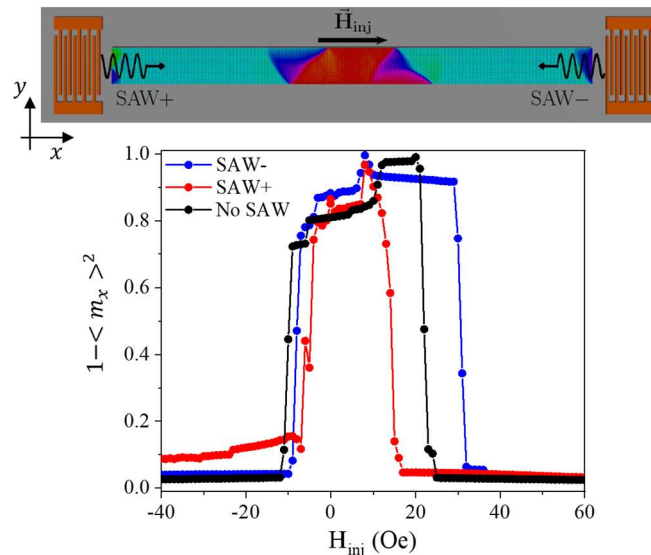


Fig. 3. (a) Sketch of the system under study consisting of a FeCo (3 nm)/Py (5 nm) nanostrip of dimensions $10 \mu\text{m} \times 1 \mu\text{m}$ on top of a piezoelectric substrate. The strip is located between two IDTs where a propagating SAW can be delivered in both x-axis directions. A reversed domain is nucleated in the center with head-to-head asymmetric transverse domain walls on both sides. (b) Computed $1 - \langle m_x \rangle^2$, signaling the presence of a DW as a function of the applied field, without a SAW (black), for a SAW of amplitude 70 ppm, traveling from left to right, SAW+, (red), and for the SAW traveling from right to left, SAW-, (blue).

In the simulations, we followed the same procedure described for the experiment. The magnetic system is initially saturated towards the negative x-direction. Then, for a given external magnetic field H_{inj} , we introduce three domains with an average $\langle m_x \rangle \approx 0$ over the entire strip. The DWs quickly relax to asymmetric transversal walls²⁸ (Fig. 3a), like the ones imaged experimentally by MFM (Fig. 1c). The presence of a DW can be estimated by computing the value of $1 - \langle m_x \rangle^2$, where m_x is the x component of the normalized magnetization. When the sample is saturated along the x-direction $1 - \langle m_x \rangle^2 \approx 0$, whereas $1 - \langle m_x \rangle^2 \approx 1$ when DWs are present. Thus, the computed equivalent to the AMR signal in the strip, also constitutes a signature of the structure of the different types of DWs, just as in the experiment.

In Fig. 3b we present the results of the simulations, where the presence of a DW is monitored as a function of the external field H_{inj} , for different directions of a SAW of amplitude 70 ppm (which is equivalent to the 18 dBm used in the experiment, as shown in Suppl. Info. S0). Without SAW, the

probability curve (black line) is very similar to the experimental one (Fig. 1e). In the absence of the SAW and for positive fields, there is a characteristic propagation field $H_{inj} = 23$ Oe, for which the probability drops to zero because both DWs are unpinned and propagate toward the ends of the strip where they annihilate. For $H_{inj} = -10$ Oe the probability drops again to zero because the pair of nucleated DWs propagate against each other, colliding and annihilating. The precise values of the propagating and annihilating fields can be slightly different in the simulation and the experiment, due to the dispersion in the experimental values for the batch of devices (Suppl. Info. S3). Also, the simulation did not include temperature, which can reduce the switching field.

Fig 3b reproduces the experimental findings when the SAW is present, as both the positive propagation field and the negative annihilation field change their value noticeably. These changes depend on the direction of travel of the SAW and the effect becomes more relevant as the amplitude of the acoustic wave ε increases. Noticeably, for $H_{inj} > 0$ and SAW +, the mobility of the DW is enhanced and, consequently, the propagation field is reduced. Similarly, for $H_{inj} > 0$ and SAW -, the DW motion is hampered, and the propagation field increases. A smaller effect with a similar qualitative explanation can be extracted for negative fields. See also Movies 1 and 2 in Supplementary Material (Refer to movie captions in the introduction of Suppl. Info.).

Given the results presented so far, both experimental and theoretical, it becomes clear that the SAW is promoting the movement of the DW in the same direction that the SAW is traveling. To clarify the underlying mechanism, we carried out a second computational study simplifying the structure of the device, as shown in Fig. 4a. Now the Permalloy layer is removed, and the simulation is done without any external magnetic field. As in the previous study, an asymmetric transverse DW is stable in the strip. The mechanical excitation is activated after the DW is stabilized at the center of the strip. Fig. 4b displays the time evolution of the position along the nanostrip, X_{DW} , for two values of the SAW amplitude ε and for both traveling directions, left to right or SAW+ and right to left or SAW-. Without SAW (black line) the DW remains at the centre ($X_{DW} = 0$) but when the SAW is present, the DW undergoes a complex oscillatory motion that results in a net displacement along the direction of the traveling SAW. The process can be visualized in the animation in Suppl. Mat. (Movie 3). In Fig. 4c we present snapshots of the magnetization configuration for different values of the amplitude of the SAW, taken at the same instant ($t = 15$ ns), showing that the DW moves along the direction in which the SAW propagates, and that the displacement increases with the amplitude of the SAW.

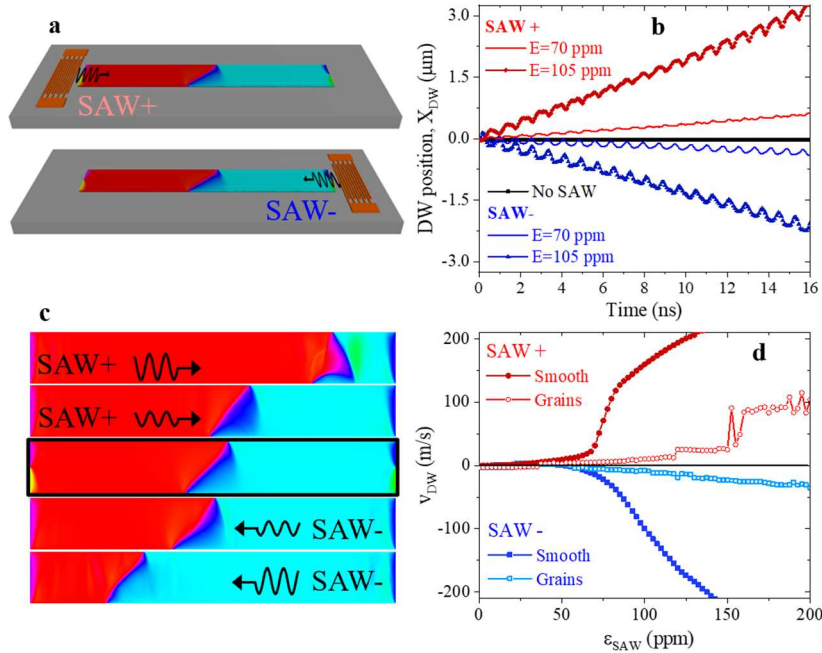


Fig. 4. (a) Set up with a single transversal DW nucleated in the middle of a FeCo strip where the SAW is delivered from both directions as indicated in the figure (b) Time evolution of the DW position along the nanostrip for several values of the SAW

amplitude and propagation direction. (c) Snapshots of the magnetization configuration 15 ns after activating the SAW, where the color scale represents the magnitude of m_x (red for $m_x = 1$, cyan for $m_x = -1$), for SAW amplitudes of 70 ppm and 105 ppm and opposite directions, as indicated in the figure. (d) DW average velocity versus the amplitude of the SAW for ideal-smooth and granular nanostrips in both SAW+ and SAW- directions.

In Fig. 4d the average DW velocity, v_{DW} , is plotted as a function of the SAW amplitude, ϵ_{SAW} , for both propagating directions. The DW speed increases monotonically with the amplitude of the SAW and three regimes can be observed. After a linear regime with a small slope for low values of ϵ_{SAW} , a rapid non-linear increase is found for intermediate values ($\epsilon_{SAW} \sim 70 - 100$ ppm) followed by a recovery of the linear regime ($\epsilon_{SAW} > 100$ ppm) with a slope more than three times higher than in the initial regime. Together with the velocity plots obtained for ideal samples (solid symbols), in Fig. 4d we also show the result obtained for samples with disorder (open symbols). Specifically, the disordered samples have a grain distribution of characteristic diameter $d = 20$ nm and standard deviation of the anisotropy constant among grains $\sigma = 3\%$. The DW velocities are significantly reduced due to the pinning introduced by the disorder and the regimes mentioned above are blurred. Nevertheless, the main effect remains: the SAW pushes the DW in the direction of its propagation. Note again that this study is done for no external magnetic field or electric current, so the movement of the DW is triggered exclusively by the action of the SAW. The velocity curves for SAW+ and SAW- are slightly different for samples with and without disorder. This difference is due to the asymmetric configuration of the DW, which is tilted with the x axis (see snapshots in Fig. 4c), which results in an asymmetric response for opposite traveling directions of the SAW. This effect is highlighted in Fig. S4 of Suppl. Inf., where the DW speed is plotted as a function of the angle between the nanostrip axis and the SAW propagation direction for the four possible DW configurations with equivalent energy. The maximum average velocity for each type of DW is obtained for a given angle showing that the SAW-induced DW motion reported in the present work, distinguishes between different DW tilt and chirality configurations. This fact may become clearer after the discussion section. We should also mention that it is the longitudinal strain wave, ϵ_{xx} the one responsible for the DW motion^{29,30}, as shown in Suppl. Inf. S5. Additionally, reducing the magnetic damping enhances the movement of the DW, as shown in Suppl. Inf. S6.

Discussion and Conclusions

In this section, we provide an intuitive explanation of this mechanism. In Figure 5a-e we plot the time evolution of the energy of the DW normalized to its energy without SAW (Fig. 5a), the width of the DW (Fig. 5b), its length (Fig. 5c), its instantaneous velocity (Fig. 5d) and the DW position (Fig. 5e). In all the panels, for clarity, we plot the longitudinal strain of the SAW ϵ_{xx} (dash black line) evaluated at the center of the moving DW. In all these panels, there is a color band around 1 ns, which marks the region where we focus this discussion.

We begin by noticing that the energy of the DW becomes maximum just after the SAW reaches its maximum stress (Fig. 5a), which coincides with the minimum in its width (Fig. 5b). At that point, the DW finds a strategy to liberate part of this accumulated magnetoelastic energy: it jumps slightly forwards (see Fig. 5e) and that allows the DW to increase its size (Fig. 5b and 5c) and reduce its energy faster than during its normal oscillatory behavior (Fig. 5a at the yellow band, just after the maximum). Although at this specific time, the instantaneous velocity of the DW changes signs momentarily, the overall effect on the instantaneous velocity (Fig. 5d) is that, in one cycle, the DW spends slightly more time with positive velocity than with negative velocity, resulting in a net displacement in the direction of the traveling SAW. The mechanism can be visualized during several cycles of the SAW in Movies 4 and 5 In Suppl. Mat., where it is visible how the DW releases part of its accumulated magnetoelastic energy through an internal wave that travels along the length of the DW as the DW ‘springs’ slightly forward. Indeed, the overall result is that the DW gains linear momentum, which is transferred from the SAW by this non-trivial mechanism.

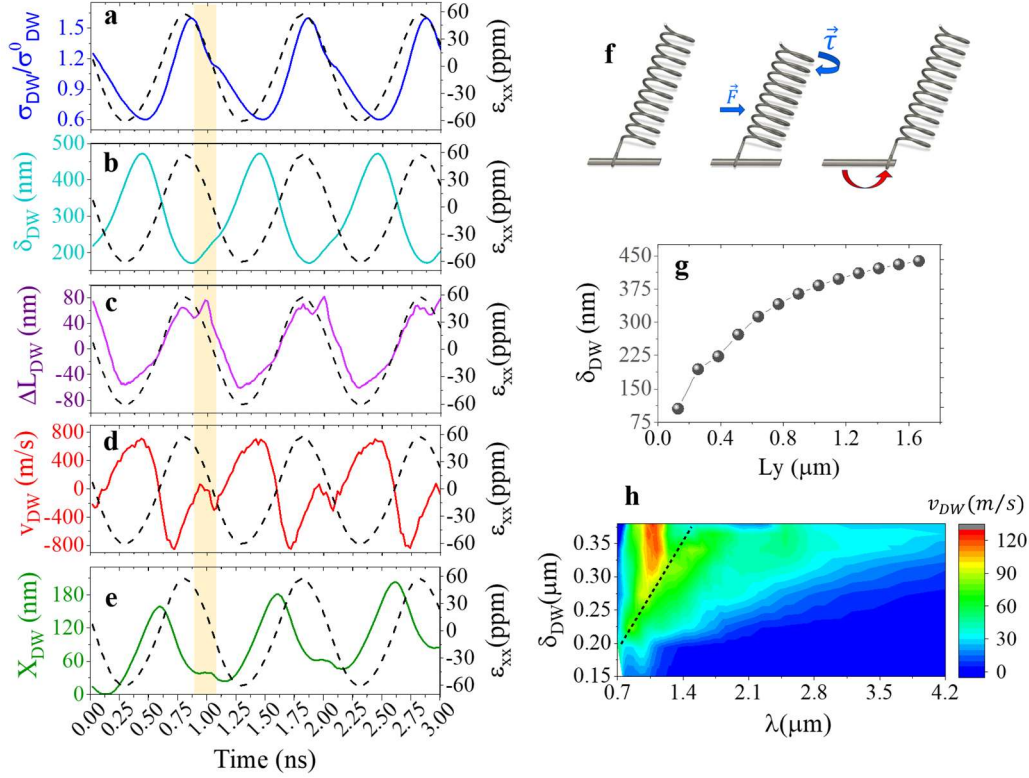


Fig. 5. (a) Time evolution of the energy of the DW normalized to its resting energy, The dotted black curve represents (in this panel and the subsequent panels) the stress of the SAW evaluated in the center of the moving DW (b) Time evolution of the width of the DW. (c) Time evolution of the length of the DW. (d) The instant velocity of the DW with time. (e) Position of the DW as a function of time. (f) The mechanical counterpart of the mechanism is described in this article. (g) Width of the DW as a function of the width of the strip. (h) Contour plot with the average velocity of the DW as a function of the width of the DW and the wavelength of the SAW. All the simulations were done for an amplitude of the SAW of $\epsilon = 70$ ppm propagating from left to right (SAW+). The dotted black straight line in the contour plot has a slope of $\lambda/4$. The relation between SAW frequency and wavelength is given by the velocity of elastic waves in CoFe, $v = \lambda f = 3640$ m/s.

Figure 5f shows a mechanical counterpart of this effect. A tilted spring is twisted while a small force pushes it towards the positive x -axis (middle image). If the accumulated stress is large enough, the spring will jump forward to release part of its elastic energy (indicated with a red arrow on the left image).

Therefore, if the right conditions are met (as discussed in the remaining part of this section), the DW moves by ‘springing’ forward in every cycle of the SAW, gaining linear momentum directly from the SAW. To make the rest of the discussion more readable, we will refer to this complex mechanism as ‘DW springing’. One can intuitively realize that, for a given amplitude of the SAW, the DW may be able to spring forward if it is wide enough in comparison to the wavelength of the SAW. To determine the importance of the size of the DW, we conducted systematic micromagnetic simulations for different wavelengths of the SAW and several widths of the strip L_y . It is important to realize that the natural width of the DW δ_{DW} , does not grow linearly with the width of the strip L_y , as shown in Figure 5g. In Figure 5h, we plot the average velocity of the DW as a function of the width of the DW δ_{DW} and the wavelength of the SAW. As can be seen, the maximum velocity is obtained, for a wavelength of $\lambda \approx 1 \mu\text{m}$, for all the strip widths evaluated. Also, the movement of the DW is almost suppressed for $\delta_{DW} \approx 0.2 \mu\text{m}$, regardless of the wavelength of the SAW. The dotted straight line in Fig. 5h represents a line with slope $\lambda/4$. It becomes clear that, for the DW to spring under the action of the SAW, its width cannot be far from 1/4 of the wavelength of the SAW. If the width of the DW is smaller or larger, the movement by springing rapidly becomes less effective or is completely suppressed. Interestingly, even for very narrow strips (and therefore narrow DWs), if the wavelength of the SAW is small enough, the DW can still move by springing, even though the average velocity

may not be relevant for moderate amplitudes of the SAW, as shown in Suppl. Inf. S7 for a very narrow strip.

It is also important to note that the DW must be asymmetric to spring under the action of the SAW. The effect of the SAW in a vortex DW can be seen in Movie 6 of Suppl. Mat. As the stress accumulated in each cycle of the SAW is symmetric across the DW, the DW only undergoes an oscillation around its position. For a large amplitude of the SAW, the DW moves a small distance (smaller than its width) after many SAW cycles. This is caused by the delay between the accumulation of magnetoelastic stress in the DW and the stress carried by the SAW¹⁹, which may produce small movements on vortex walls or skyrmions but are too small for any practical purpose.

Finally, and importantly, the SAW uses 0.2 nW of power to move the DW. This value is obtained from the average energy that the DW releases by springing per cycle of the SAW. If we consider the resistance of the $\sim 1\mu\text{m}$ long strip section where the DW is sitting ($\sim 10\ \Omega$), an equivalent power would be obtained for a current density of $\sim 4.5 \cdot 10^4\ \text{A/cm}^2$, which is considerably smaller than the current density required to move DWs or to switch nanostructures by Spin-Orbit Torque^{31,32}, usually in the range of $10^7\ \text{A/cm}^2$.

We can conclude that the mechanism described in this article, through which the SAW can directly transfer linear momentum to the DW, potentially, without any external field or current, may well be the base of many future spintronic devices. By synchronizing the acoustic waves from different directions, it will be possible to move the DW between pre-defined positions, with a small energy cost compared to existing methods to move the DW without external fields.

References

1. Goldie, J.H., Gerver, M.J., Oleksy, J., Carman, G.P. & Duenas, T.A. Composite Terfenol-D sonar transducers Proc. SPIE 3675, Smart Structures and Materials (1999).
2. Kim, CK. & O'Handley R.C. Development of a magnetoelastic resonant sensor using iron-rich, nonzero magnetostrictive amorphous alloys. Metall. Mater. Trans. A **27**, 3203 (1996).
3. Prieto, J.L., Aroca, C., Lopez, E., Sanchez, M.C. & Sanchez, P. Magnetostrictive-piezoelectric magnetic sensor with current excitation. J. Mag. Mag. Mat. **215**, 756 (2000).
4. Puebla, J., Hwang, Y., Maekawa, S. & Otani Y. Appl. Phys. Lett. **120**, 220502 (2022).
5. Weiler, M. et al. Elastically driven ferromagnetic resonance in nickel thin films. Phys. Rev. Lett. **106**, 117601 (2011).
6. Weiler, M. et al. Spin pumping with coherent elastic waves. Phys. Rev. Lett. **108**, 176601 (2012).
7. Thevenard, L. et al. Precessional magnetization switching by a surface acoustic wave. Phys. Rev. B. **93**, 134430 (2016).
8. Tejada, J. et al. Switching of magnetic moments of nanoparticles by surface acoustic waves. Eur. Phys. Lett. **118**, 37005 (2017).
9. Sampath, V. et al. Acoustic-wave-induced magnetization switching of magnetostrictive nanomagnets from single-domain to non-volatile vortex states. Nano. Lett. **16**, 5681-5687 (2016).
10. Li, W., Buford, B., Jander, A. & Dhagat, P. Acoustically assisted magnetic recording: a new paradigm in magnetic data storage. IEEE Trans. Mag. **50**, 3100704 (2014).
11. Biswas, A. K., Bandyopadhyay, S. & Atulasimha, J. Acoustically assisted spin-transfer-torque switching of nanomagnets: An energy-efficient hybrid writing scheme for non-volatile memory. Appl. Phys. Lett. **103**, 232401 (2013).
12. Chen, R. et al. Ordered creation and motion of skyrmions with surface acoustic wave. Nat. Commun. **14**, 4427 (2023). <https://doi.org/10.1038/s41467-023-40131-1>
13. Slonczewski, J. C. Current driven excitations of magnetic multilayers. J. Magn. Magn. Mater. **159**, L1 (1996).
14. Edrington, W. et al. SAW assisted domain wall motion in Co/Pt multilayers. Appl. Phys. Lett. **112**, 052402 (2018).
15. Castilla D. et al. Magnetization process of a ferromagnetic nanostrip under the influence of a surface acoustic wave. Scientific Reports, **10**:9413 (2020).
16. Adhikaria, A. & Adenwalla, S. Surface acoustic waves increase magnetic domain wall velocity. AIP Advances **11**, 015234 (2021).

17. Ramos, E., López, C., Akerman, J., Muñoz, M., Prieto J.L. Joule heating in ferromagnetic nanostripes with a notch. *Phys. Rev. B.* **91**, 214404 (2015).
18. López, C. et al. Influence of the thermal contact resistance in current-induced domain wall depinning. *J. Phys. D: Appl. Phys.* **50**, 325001 (2017).
19. Dean, J. et al. A sound idea: Manipulating domain walls in magnetic nanowires using surface acoustic waves. *Appl. Phys. Lett.* **107**, 142405 (2015).
20. Yang, Y. et al. Acoustic-driven magnetic skyrmion motion. *Nat. Commun.* **15**, 1018 (2024).
21. Hayashi, M. et al. Dependence of current and field driven depinning of domain walls on their structure and chirality in permalloy nanowires. *Phys. Rev. Lett.* **97**, 207205 (2006).
22. Muñoz, M. & Prieto, J.L. Suppression of the intrinsic stochastic pinning of domain walls in magnetic nanostripes. *Nat. Commun.* **2**:562 (2011).
23. Proenca, M. et al. Deterministic and time resolved thermo-magnetic switching in a nickel nanowire. *Scientific Reports* **9**:17339 (2019).
24. Hayashi, M. et al. Influence of current on field-driven domain wall motion in permalloy nanowires from time resolved measurements of anisotropic magnetoresistance. *Phys. Rev. Lett.* **96**, 197207 (2006).
25. Hayashi, M., Thomas, L., Rettner, C., Moriya, R. & Parkin, S.S.P. Direct observation of the coherent precession of magnetic domain walls propagating along permalloy nanowires. *Nature Phys.* **3**, 464 (2007).
26. Prieto, J.L., Muñoz, M., & Martínez E. Structural characterization of magnetic nanostripes by fast domain wall injection. *Phys. Rev. B.* **83**, 104425 (2011).
27. Vansteenkiste, A. et al. The design and verification of MuMax3. *AIP Advances* **4**, 107133 (2014).
28. Nakatani, Y., Thiaville, A. & Miltat, J. Head-to-head domain walls in soft nano-strips: a refined phase diagram. *J. Mag. Mag. Mat.* **290-291**, 750 (2005).
29. Edrington, W. et al. SAW assisted domain wall motion in Co/Pt multilayers,” *Appl. Phys. Lett.* **112**(5), 052402 (2018).
30. Cao, Y. et al. *Appl. Phys. Lett.* **119**, 012401 (2021).
31. Bhowmik, D. et al. Deterministic domain wall motion orthogonal to current flow due to Spin Orbit Torque. *Sci Rep* **5**, 11823 (2015).
32. Krizakova, V., Perumkunnil, M., Couet, S., Gambardella, P., & Garello, K. Spin-orbit torque switching of magnetic tunnel junctions for memory applications. *J. Mag. Mag. Mat.* **562**, 169692 (2022).

Acknowledgments

This work has received funding from the Spanish Ministry of Science and Innovation through projects PID2020-117024GB-C4, PID2020-117024GB-C41 and 2D-SAWNICS (PID2020-120433GB-I00).

Methods

In the micromagnetic simulations, we assume that the SAW is a pure Rayleigh wave, which consists of both longitudinal (σ_{xx} and σ_{zz}) and shear stress (σ_{xz}) propagating waves, such as those described in [19]. The stress waves are linked to the corresponding strain waves (ε_{xx} , ε_{zz} and ε_{xz}) through the elastic constants. In addition, we assume that the strain in the SAW is transferred entirely to the magnetic nanostrip and that the Rayleigh waves propagate without dissipation while traveling through it. Also, magnetostriction, the mechanical strain induced by the magnetic configuration, is neglected. Therefore, the acoustic excitation propagating along the x axis can be as

$$\begin{aligned}\varepsilon_{xx}(x, t) &= E \sin(kx - \omega t) \\ \varepsilon_{zz}(x, t) &= -E \sin(kx - \omega t) \\ \varepsilon_{xz}(x, t) &= E' \sin(kx - \omega t + \pi/2) \\ \varepsilon_{yy}(x, t) &= \varepsilon_{yx}(x, t) = \varepsilon_{yz}(x, t) = 0\end{aligned}$$

where E , ω and k are the SAW amplitude, frequency, and wave vector, respectively. In this work $f = 1.3$ GHz and $\lambda = \frac{2\pi}{k} = 2.8$ μm except in Fig. 5c, where both ω and λ are changed according to the dispersion relation $v = \lambda f = 3656$ m/s. Propagation along the positive (negative) x -direction corresponds to $k > 0$ ($k < 0$). The labels x , y , and z refer to the coordinate system depicted in Fig.3. The effect of SAW on the magnetization is taken care of via the magnetoelastic field

$$\vec{H}_{mel} = -\frac{2}{\mu_0 M_S} \begin{bmatrix} B_1 m_x \varepsilon_{xx} + B_2 (m_y \varepsilon_{xy} + m_z \varepsilon_{xz}) \\ B_1 m_y \varepsilon_{yy} + B_2 (m_x \varepsilon_{xy} + m_z \varepsilon_{yz}) \\ B_1 m_z \varepsilon_{zz} + B_2 (m_x \varepsilon_{xz} + m_y \varepsilon_{yz}) \end{bmatrix}$$

where B_1 and B_2 are the magneto-elastic constants, and $\vec{m} = \vec{M}/M_S$ is the normalized magnetization.

The following material parameters were used for FeCo and Py, respectively: exchange constant $A_{\text{FeCo}} = 10.5$ pJ/m, $A_{\text{Py}} = 13$ pJ/m; saturation magnetization $M_{s,\text{FeCo}} = 1.5$ MA/m, $M_{s,\text{Py}} = 0.8$ MA/m; in-plane anisotropy constant $K_{\text{FeCo}} = 7$ kJ/m³, $K_{\text{Py}} = 0$ kJ/m³ (easy axis along x direction) and Gilbert damping constant $\alpha_{\text{FeCo}} = 0.02$, $\alpha_{\text{Py}} = 0.02$. The same magnetoelastic constant values $B_1 = B_2 = -84$ MPa were used for both FeCo and Py and we assumed that the strain induced by the SAW in the PZ is fully transmitted to both magnetic layers. The nanostrip is discretized $4 \times 4 \times 3$ nm³ cells. The grain structure is set using the Voronoi tessellation implemented in mumax3. The average grain diameter is $d = 20$ nm and both the in-plane anisotropy constant and easy-axis orientation are randomly distributed among the different grains following a Gaussian distribution around their nominal values with standard deviation $\sigma = 3\%$.